Isovalent vs. Aliovalent Transition Metal Doping of Zinc Oxide Lithium-Ion Battery Anodes – In-Depth Investigation by *ex situ* and *operando* X-ray Absorption Spectroscopy

Angela Trapananti,[a,*] Tobias Eisenmann,[b,c] Gabriele Giuli,[d] Franziska Mueller,[b,c] Arianna Moretti,[b,c] Stefano Passerini,[b,c] and Dominic Bresser [b,c,*]

[a] *School of Science and Technology, Physics Division, University of Camerino, 62032 Camerino, Italy*

[b] *Helmholtz Institute Ulm (HIU), Helmholtzstrasse 11, 89081, Ulm, Germany*

[c] *Karlsruhe Institute of Technology (KIT), P.O. Box 3640, 76021 Karlsruhe, Germany*

[d] *School of Science and Technology, Geology Division, University of Camerino, 62032 Camerino, Italy*

Abstract

The precise determination of de-/lithiation mechanisms in alternative lithium-ion battery electrode materials is crucial for their potential future success, but quite challenging – e.g., due to the occurrence of multiple crystalline and (frequently) amorphous phases. Herein, we report an in-depth *ex situ*/*operando* characterization of (carbon-coated) Fe-doped and Co-doped zinc oxide anodes via X-ray absorption spectroscopy to probe the oxidation state and local structural environment of the different metals upon de-/lithiation. The results provide fundamental insights into the mechanism of the conversion and alloying reaction taking place for these two active materials. In addition, this comparative investigation allows for an evaluation of the impact of isovalent (Co^{2+}) and aliovalent (Fe^{3+}) doping on the lithiation mechanism, having an impact on the initial lithiation kinetics, while both dopants generally enable a greatly increased re-oxidation of zinc compared to pure zinc oxide and, thus, a more reversible conversion reaction.

***Corresponding authors:** angela.trapananti@unicam.it ; dominic.bresser@kit.edu

1. Introduction

Lithium-ion batteries (LIBs) are the state-of-the-art power source for portable consumer electronics as well as stationary energy storage devices and (hybrid) electrical vehicles [1,2]. This tremendous success and steadily increasing sales of LIB cells, however, are coming along with an increasing need to tailor the properties of the battery cells towards the specific application targeted and to diversify the active material chemistry in order to warrant a sufficient supply also in the mid-term to long-term future [3,4]. With regard to the negative electrode, most alternative active materials are reversibly hosting lithium via an alloying [5–11] and/or conversion mechanism [12–19]. Especially, the conversion mechanism and the combined conversion/alloying mechanism, however, are still not fully understood. Remaining questions are, for instance, dealing with the origin of the voltage hysteresis, the factors determining the electrolyte decomposition and the stability of the initially formed solid electrolyte interphase (SEI), as well as the requirements to achieve a highly reversible Li_2O formation. The latter is particularly hampered when using "simple" alloying metal oxides such as ZnO or SnO_2, resulting in a rapid initial capacity fading and low Coulombic efficiencies [12–15,20], which renders the potential of these materials for application in lithium-ion cells (i.e., with the cathode active material being the only lithium source) very limited. To overcome this issue, the incorporation of 3d transition metals (TMs), e.g., Fe or Co, has been reported as viable strategy, allowing for long-term stable cycling of such materials at specific capacities equivalent or close to the theoretical maximum [21–28]. The general reaction mechanism was investigated by *operando* X-ray diffraction (XRD) studies, revealing that the presence of the TM confines the initially formed zinc or tin nanograins to the nanoscale. This appears essential for maintaining a high reversibility of the conversion-type contribution [24,26–28]. Nevertheless, the (quasi-)amorphous state and (sub-)nanoscale size of the different electrochemically active phases limit the information depth provided by XRD, especially concerning the "XRD invisible" transition metals. Particularly, insights into the redox

behavior and local structure of the TMs appear of utmost importance for a better understanding of the impact of the dopant on the overall de-/lithiation mechanism. X-ray absorption spectroscopy (XAS) has been successfully used in recent years to better understand the impact of the TM dopant on the pristine crystal structure in the case of zinc oxides [29]. An *ex situ* study of the lithiation at elevated potentials revealed that the initial reduction of Fe^{3+} to Fe^{2+} is accompanied by an insertion of lithium cations into the cationic vacancies resulting from the aliovalent doping [30]. Nonetheless, the evolution of the electronic and local structure during a complete lithiation and, moreover, upon the subsequent delithiation is still missing.

Herein, we provide such comprehensive *ex situ* and *operando* XAS analysis – not only for Fe-doped, but also for Co-doped ZnO. The resulting X-ray absorption near edge structure (XANES) spectra and the extended X-ray absorption fine structure (EXAFS) spectra enlighten the electrochemical de-/lithiation mechanism of such TM-doped zinc oxides, revealing important insights into the electronic state of the TM dopants and zinc (XANES) as well as into the local atomic environment (EXAFS) as a function of the state of charge. The direct comparison of Fe and Co additionally allows for critical information regarding the impact of the initial oxidation state of the TM, which is considered important for the general understanding of conversion and conversion/alloying materials and their de-/lithiation mechanism.

2. Experimental Section

2.1 Synthesis

$Zn_{0.9}Fe_{0.1}O$ and $Zn_{0.9}Co_{0.1}O$ were synthesized by dissolving zinc (II) gluconate hydrate (ABCR) and either iron (II) gluconate dihydrate (Sigma Aldrich) or cobalt (II) gluconate hydrate (ACROS ORGANICS) in ultra-pure water (Millipore). The total metal ion concentration was 0.2M with a molar Zn:TM ratio of 9:1. Subsequently, this solution was added dropwise to an aqueous 1.2M solution of

sucrose (Acros Organics). After stirring at RT for about 15 min the water was evaporated at 160 °C, before increasing the temperature further to 300 °C to initiate the decomposition of the sucrose. The resulting solid precursor was calcined under air for 3 h at 450 °C in the case of $Zn_{0.9}Fe_{0.1}O$ and at 400 °C in the case of $Zn_{0.9}Co_{0.1}O$ using a tubular furnace (Nabertherm). The heating rate was set to 3 °C min^{-1}. For the application of the carbon coating, the $Zn_{0.9}Fe_{0.1}O$ powder was manually ground and subsequently dispersed in an aqueous sucrose solution. The weight ratio of $Zn_{0.9}Fe_{0.1}O$ to sucrose was 1:1. The dispersion was homogeneously mixed by means of planetary ball milling (Vario-Planetary Mill Pulverisette 4, Fritsch). The water was evaporated at 80 °C under ambient atmosphere and the resulting solid material was briefly ground prior to an annealing step at 500 °C for 4 h under an inert argon gas flow of 750 mL min^{-1} (tubular furnace, Nabertherm). Finally, the material was ground once more to obtain a fine powder. The carbon content in carbon-coated $Zn_{0.9}Fe_{0.1}O$ ($Zn_{0.9}Fe_{0.1}O$-C) was determined to be 20 wt.% by thermogravimetric analysis (TGA, TA Instruments Discovery).

2.2 Electrode Preparation and Electrochemical Characterization

Electrodes were prepared by dissolving polyvinylidene difluoride (PVdF, Kynar 761, Arkema) in *N*-methyl-2-pyrrolidone (NMP, Aldrich), and subsequently adding the conductive carbon (Super C65®, IMERYS) and the active material. The dispersion was homogenized by ball milling (4x 30 min at 400/-800 rpm with 10 min rest in-between each milling step). The resulting slurry was cast onto carbon paper (QuinTech) serving as current collector. The wet film thickness was adjusted to 300 µm by using a laboratory-scale doctor blade. The electrode sheet was dried at room temperature before cutting disc-shaped electrodes with a diameter of 12 mm. Finally, these electrodes were dried under vacuum at 120 °C for 24 h. The overall composition of the electrodes was 70 wt.% of the active material, 20 wt.% of

conductive additive, and 10 wt.% of binder. The electrode active material mass loading was in the range of 4.5 to 7.0 mg cm^{-2}.

For the *ex situ* XAS analysis, three-electrode Swagelok® cells were assembled in an argon-filled glove box (MBraun; H_2O and O_2 content; < 0.1 ppm) using lithium foil (Honjo, battery grade) as reference and counter electrodes. Accordingly, all potential values given herein refer to the Li^+/Li redox couple. Six layers of a polypropylene fleeces (Freudenberg FS 2190) served as separator, which were drenched with 150 µL of 1M $LiPF_6$ in a 3:7 wt./wt. mixture of ethylene carbonate and diethyl carbonate (UBE), serving as the electrolyte. The electrodes based on $Zn_{0.9}Fe_{0.1}O$-C and $Zn_{0.9}Co_{0.1}O$ were galvanostatically lithiated and delithiated to specific cut-off potentials employing a Maccor Battery Tester 4300 with a dis-/charge rate of C/20 (1C = 1000 mA g^{-1}). The temperature was fixed to 20 ± 2 °C using a climatic chamber (Binder). Subsequently, the cells were disassembled inside the argon-filled glove box to recover the electrodes, which were then washed with dimethyl carbonate to remove the electrolyte, vacuum-dried, sealed in transparent polyethylene foil, and, lastly, sealed in an airtight pouch bag for the transport to the synchrotron.

For the *operando* XAS measurements, two-electrode pouch bag cells were assembled using 50 µm thin lithium foil (Honjo, battery grade) as counter electrode. The counter and the working electrode (based on the active material) were separated by a Separion separator (Evonik) drenched with the same electrolyte as used for the *ex situ* studies. Simultaneous to the XAS measurements galvanostatic cycling was performed using a CH Instruments 660B potentiostat for the investigation of $Zn_{0.9}Fe_{0.1}O$-C and a VSP-150 single channel potentiostat (BioLogic) for $Zn_{0.9}Co_{0.1}O$. In both cases, the cells were cycled with a dis-/charge rate of around C/10 (1C = 1000 mA g^{-1}), with minor adjustments depending on the available beam time.

2.3 X-ray Absorption Spectroscopy

The *ex situ* and *operando* XAS measurements were performed at the Italian beamline (LISA-BM08) of the European Synchrotron Radiation Facility (ESRF, Grenoble, France). The Fe, Co, and Zn K-edge spectra (XANES and EXAFS) were collected in transmission mode. A fixed-exit double-crystal Si (311) monochromator was used to monochromatize and horizontally focus the white beam delivered by the bending magnet source. Two palladium-coated mirrors, set at an incidence angle of 3.6 mrad, were used for harmonic rejection. The intensities of the incident and transmitted beams were recorded using ionization chambers filled with argon gas at different pressures to optimize the efficiencies at the different working energies. Fe, Co, and Zn metal foils were utilized for the initial X-ray beam energy calibration (by defining the first inflection point in the metallic Fe, Co, and Zn spectra as 7112, 7709, and 9659 eV, respectively). Spectra of these reference foils were measured simultaneously with any sample at the respective element edge for the proper monitoring of the energy scale. The experimental data were treated with the Demeter package [31] for the energy calibration, normalization, background subtraction, extraction of the EXAFS data as well as the quantitative structural refinement. According to standard procedures implemented within the Artemis software, the k^2-weighted EXAFS spectra $\chi(k)$ were Fourier-transformed in a *k*-range of 3.0-11.5 $Å^{-1}$ for the Fe and Co K-edges and in a range of 2-12 $Å^{-1}$ for the Zn K-edge with a Kaiser-Bessel window function. The fitting was performed in the R-space and the theoretical backscattering amplitudes and the phase shifts were calculated using the FEFF6 code [32]. Fitting parameters were the scattering path length *R* and the EXAFS Debye-Waller factor σ^2 for each path, the E_0 shift, and the amplitude reduction factor S_0^2. The latter was determined by fitting the corresponding metal references.

3. Results and Discussion

3.1 General Properties of $Zn_{0.9}Fe_{0.1}O$(-C) and $Zn_{0.9}Co_{0.1}O$

A comprehensive physicochemical characterization of the as-synthesized nanoparticulate $Zn_{0.9}Fe_{0.1}O$(-C) and $Zn_{0.9}Co_{0.1}O$ active materials has been reported in several earlier studies on these materials [24,25,27–30,33]. Of importance for the investigation presented herein are the following findings: The nanoparticles have a diameter of about 10-20 nm, the materials are phase-pure with a wurtzite crystal structure, and both iron and cobalt cations are successfully introduced into the lattice substituting Zn^{2+} in tetrahedral sites. The incorporated iron is purely trivalent in the case of $Zn_{0.9}Fe_{0.1}O$ and about 95% trivalent in the case of $Zn_{0.9}Fe_{0.1}O$-C (with 5% divalent iron), while cobalt is purely divalent in $Zn_{0.9}Co_{0.1}O$ [29]. The aliovalent Fe^{3+} doping leads to cationic vacancies, which enable an initial Li^+ insertion into the wurtzite crystal structure at elevated potentials, accompanied by the reduction of Fe^{3+} to Fe^{2+}, prior to the onset of the conversion reaction [30]. The overall reaction mechanism, though, is essentially the same for $Zn_{0.9}Fe_{0.1}O$ and $Zn_{0.9}Fe_{0.1}O$-C [24,27], while the carbon coating enables stable cycling, *inter alia* thanks to the stabilization of the electrode|electrolyte interface [34]. Generally, both materials $Zn_{0.9}Fe_{0.1}O$-C and $Zn_{0.9}Co_{0.1}O$ reveal stable cycling with specific capacities around the theoretical maximum of about 960 mAh g^{-1} [24,25,28]. For this reason and the fact that the focus of the present study is on the changes occurring in the bulk material, we have chosen these two compounds for the investigation presented herein. Two exemplary first cycle potential profiles of electrodes based on $Zn_{0.9}Co_{0.1}O$ and $Zn_{0.9}Fe_{0.1}O$-C (cycled in half-cell configuration) are shown in **Figure 1**, with an indication of the potential values at which the cells were stopped for the *ex situ* XAS analysis. Both potential profiles reveal the characteristic shape for these two materials with a rather large initial irreversible capacity due to the high surface area and the formation of the SEI at the electrode|electrolyte interface [34].

3.2 Ex situ XANES Spectroscopy

We may start with a qualitative discussion of the *ex situ* XANES spectra recorded at the Co and Fe K-edge, which are displayed in **Figure 2** (compare also **Figure S1a,b**). The spectra obtained for the pristine electrodes are very well matching the spectra reported for the corresponding powders with Co^{2+} and Fe^{3+} in the tetrahedral sites of wurtzite ZnO [29]. Especially the dominant pre-edge peaks in both cases are a good indication for such successful doping and replacement of Zn^{2+} by the two TMs in the tetrahedral sites of the wurtzite lattice. Globally, upon lithiation, the main edge positions shift towards lower energies, which is related to the reduction of Co^{2+} to Co^0 (**Figure 2a**) and Fe^{3+} to Fe^0 (**Figure 2b**), while a closer look at the pre-edge peaks at the Fe K-edge during the initial stages of lithiation in the inset of **Figure S1b** confirms that Fe^{2+} is intermediately formed [30]. A more detailed comparison of both materials shows that at 0.8 V, the spectrum of the Co K-edge appears rather similar to the pristine one, indicating an unchanged oxidation state, while Fe is already fully reduced. In fact, this finding is not intuitive with regard to the standard redox potentials of Fe^{2+}/Fe^0 (-0.44 V) and Co^{2+}/Co^0 (-0.28 V) in an aqueous solution vs. the standard hydrogen electrode (SHE). Nonetheless, the specific capacity at such potential is much lower for $Zn_{0.9}Co_{0.1}O$ (ca. 100 mAh g^{-1}) compared to 230 mAh g^{-1} in the case of $Zn_{0.9}Fe_{0.1}O$-C. This finding is in line with the initial Li^+ insertion at elevated potentials due to the presence of aliovalent iron and the subsequently favored further reduction of iron to the metallic state [30]. The metallic nanograins then serve as nucleation sites for the formation of an FeZn alloy along with the reduction of zinc, as earlier found by *ex situ* Mößbauer spectroscopy [27], which additionally contributes to the higher specific capacity recorded for $Zn_{0.9}Fe_{0.1}O$-C compared to $Zn_{0.9}Co_{0.1}O$ at such an early stage of lithiation. In the fully lithiated state, though, at 0.01 V, the oscillations of both the Co and Fe XANES spectra are highly damped compared to the corresponding metal references (dashed lines), which

indicates either very small or highly defective metallic nanograins (we will get back to this later again). In the fully delithiated state at 3.0 V, the spectra eventually reveal a partial reoxidation of both Co and Fe.

Zn K-edge *ex situ* XANES spectra are shown in **Figure 3a** and **Figure 3b** for $Zn_{0.9}Co_{0.1}O$ and $Zn_{0.9}Fe_{0.1}O$-C, respectively (see also **Figure S1c,d**). Also in this case the spectra recorded for the pristine electrodes are matching very well with the ones reported earlier for the corresponding powders and display the characteristic spectral features of wurtzite ZnO [29]. In line with the spectra obtained at the Co and Fe K-edge at 0.8 V upon lithiation, the Zn K-edge spectrum of $Zn_{0.9}Co_{0.1}O$ is similar to the pristine one, while the spectrum of $Zn_{0.9}Fe_{0.1}O$-C indicates a partial reduction of zinc. This observation further confirms the facilitated conversion reaction in the case of $Zn_{0.9}Fe_{0.1}O$-C. At 0.55 V (for Co) and 0.5 V (for Fe), i.e., data points after the (sloped) potential plateau assigned to the conversion reaction, the Zn spectra show the typical features of metallic Zn^0 (though more damped – just like the spectra at the Co and Fe K-edge). Upon further lithiation, the shape of the spectra changes slightly, indicating the formation of the Li_xZn alloy. A close-up of the two fully lithiated spectra for Co-doped and Fe-doped ZnO and the Zn^0 reference (dashed line), displayed in **Figure 3c**, shows indeed that the main edge position is slightly shifted to lower values for the two lithiated electrodes, which suggests the formation of such Li_xZn alloy, as previously reported for pure ZnO [20].

For the fully delithiated electrodes, the Zn K-edge spectra of both $Zn_{0.9}Fe_{0.1}O$-C and $Zn_{0.9}Co_{0.1}O$ almost entirely recover the spectral features of the oxide phase, indicating a high degree of reconversion from Zn^0 to Zn^{2+}.

In order to quantify the results, we conducted linear combination fitting (LCF). The XANES spectra of the pristine electrode, the fully lithiated electrode, and metallic Zn^0 were used as standards for the Zn^{2+}, Li_xZn, and Zn^0 phases, respectively. The general quality of the fits with such standards was good, as

confirmed by R-factors below 0.002 in all cases. The fitting results are tabulated in **Table S1** ($Zn_{0.9}Co_{0.1}O$) as well as **Table S2** ($Zn_{0.9}Fe_{0.1}O$-C) and exemplary fits are shown in **Figure S1**. The overall results are illustrated in **Figure 3d,e**. **Figure 3d** displays the LCF results for $Zn_{0.9}Co_{0.1}O$. At 0.8 V upon lithiation, 95% of Zn is still oxidized. After the conversion reaction, i.e., at 0.55 V, it is essentially reduced completely to the metallic state. This confirms that the conversion is completed during the long potential plateau, as suggested earlier by *operando* XRD experiments revealing the disappearance of the wurtzite-related reflections [28]. Subsequently, it remains metallic until the cell has been delithiated up to 1.0 V, for which a slight decrease of the fraction of metallic zinc is observed. When further delithiating the electrode to 1.6 V, around 50% of the zinc is already reoxidized to Zn^{2+}. At 3.0 V, finally, about 80% of the zinc has been reoxidized to Zn^{2+}. This fraction is substantially higher than what has been reported for pure ZnO,[20] highlighting the beneficial impact of the TM dopant on the reversibility of the conversion reaction. In **Figure 3e**, the same analysis is provided for $Zn_{0.9}Fe_{0.1}O$-C. As qualitatively discussed above, but quantified now by LCF, around 50% of the zinc has been already reduced at 0.8 V, presumably triggered by the early reduction of iron to the metallic state. This is a quite substantial amount, reflected also by the much higher capacity at such potential compared to $Zn_{0.9}Co_{0.1}O$. After the two potential plateaus, i.e., at 0.5 V, zinc has been fully reduced to the metallic state and remains metallic during the further lithiation (including the formation of the LiZn alloy). Upon delithiation at 1.5 V, around 30% of the zinc has been reoxidized. At 3.0 V, the fraction of the reoxidized zinc is almost 80%, i.e., essentially the same value as observed for $Zn_{0.9}Co_{0.1}O$, revealing that both TM dopants have the same beneficial impact on the reversibility of the conversion reaction.

3.3 Operando XANES Spectroscopy

To confirm that the *ex situ* data are well reflecting the actual processes occurring for the active material, we combined the *ex situ* analysis with a series of *operando* experiments. Such complementary analysis rules out any potential impact of the sample preparation for the *ex situ* samples and accidental exposure to the ambient atmosphere. On the other hand, the signal to noise ratio and the range of the EXAFS signal is in general lower for the *operando* experiments due to the limited measurement time for repeated acquisition and the more complex (and highly absorbing) sample environment. The results are presented in **Figure 4**. **Figure 4a** depicts the *operando* XANES measurements at the Co K-edge for $Zn_{0.9}Co_{0.1}O$. Cobalt is gradually reduced during the initial lithiation and essentially metallic at around 50% of the total discharge capacity. The reduction of zinc to the metallic state is completed slightly later (**Figure 4b**), indicating that the reduction of cobalt during the conversion reaction is slightly preferred over the reduction of zinc – presumably due to the higher standard redox potential [35]. In the case of $Zn_{0.9}Fe_{0.1}O$-C (**Figure 4c,d**), this effect is even more pronounced and iron is completely reduced to the metallic state already at a rather early stage of the lithiation reaction (**Figure 4c**), while zinc is solely metallic at a much later stage (**Figure 4d**). This general trend is in very good agreement with the *ex situ* XANES data (**Figure 2**) and, thus, confirms the suitability of these data for a detailed analysis. Remarkably, moreover, the direct comparison of the *operando* Zn K-edge data recorded for $Zn_{0.9}Co_{0.1}O$ (**Figure 4b**) and $Zn_{0.9}Fe_{0.1}O$-C (**Figure 4d**) highlights that the presence of metallic iron at an early stage of the lithiation reaction favors also the reduction of zinc, which is completed significantly earlier in the case of $Zn_{0.9}Fe_{0.1}O$-C.

3.4 Qualitative ex situ EXAFS Analysis

Along with the *ex situ* XANES measurements, we subjected the cycled electrodes also to an extended *ex situ* EXAFS spectroscopy investigation in order to obtain also information about the local structural

evolution around the Fe, Co, and Zn absorbers. **Figure 5** shows the Fourier transform of the $k^2\chi(k)$ EXAFS spectra measured at the Co and Fe K-edges (**Figure 5a,b**) as well as the Zn K-edges (**Figure 5c,d)** of $Zn_{0.9}Co_{0.1}O$ and $Zn_{0.9}Fe_{0.1}O$-C. Zinc is tetrahedrally coordinated by oxygen with Zn-O distances of about 1.98 Å within the wurtzite ZnO crystal. The second coordination shell is composed of overall 12 Zn atoms, with six being at a distance of around 3.21 Å and another six at around 3.25 Å [29]. Since both Co^{2+} and $Fe^{3+/2+}$ replace Zn^{2+} in the lattice, there is no significant impact on such distances by the introduction of the dopants and the spectra recorded for the pristine electrodes show two dominant peaks representing this first and second coordination shell. Besides – just like for the XANES data – the EXAFS spectra are in very good agreement with the spectra obtained for the corresponding powders [29].

The EXAFS spectra collected at the Co K-edge of $Zn_{0.9}Co_{0.1}O$ are presented in **Figure 5a**. At 0.8 V, cobalt is still predominantly oxidized, as indicated by the presence of the two characteristic peaks [29], which is in good agreement with the *ex situ* XANES data (**Figure 2a**). Upon further lithiation, the EXAFS spectra show only one peak of Co^0 (compare **Figure S2a**) up to a potential of 1.6 V upon delithiation. At higher potentials (i.e., at 2.5 and 3.0 V) upon delithiation, cobalt is increasingly reoxidized. The shape and peak positions of the spectrum at 3.0 V appears similar to Zn K-edge spectrum (**Figure 5b**), which suggests that the reoxidized Co^{2+} occupies a similar position as Zn^{2+} in the oxide lattice, although the formation of CoO_x-like phases cannot be safely excluded at this point. Interestingly, the onset for the reoxidation of zinc is observed already at 1.6 V, which is in line with the previous observation by XANES that zinc is reduced later (and accordingly oxidized earlier).

The EXAFS spectra collected at the Fe K-edge of $Zn_{0.9}Fe_{0.1}O$-C are shown in **Figure 5c**. Generally, the amplitude of the peak for the second coordination shell of the pristine sample is highly damped. This is possibly due to local defects such as cationic vacancies triggered by the aliovalent Fe^{3+} doping. [29,30].

In good agreement with the XANES data, the spectrum at 0.8 V is indicating an essentially fully reduced iron, which does not change until the fully delithiated state at 3.0 V, for which a superposition of several peaks is observed, indicating a partial reoxidation. However, the degree of reoxidized iron appears slightly less than for cobalt (in line with the previous findings). Moreover, the absence of a clear pre-edge feature in the XANES spectrum (**Figure 2b**) suggests that the oxidized phase does not contain Fe^{3+} in tetrahedral sites, as in the pristine material, but rather indicates that other FeO_x phases and very fine metallic Fe nanograins are formed/present.

The Zn K-edge EXAFS spectra (**Figure 5d**) generally follow the same trend as the ones recorded for $Zn_{0.9}Co_{0.1}O$ (**Figure 5b**). Upon lithiation, the spectra follow the same trend as observed *via* XANES with the reduction of Zn^{2+}, resulting in only one peak related to the metallic zinc and, eventually, the Li_xZn alloy. The comparison of the EXAFS spectra at the Zn K-edge of $Zn_{0.9}Co_{0.1}O$ and $Zn_{0.9}Fe_{0.1}O$-C at 0.8 V upon lithiation, moreover, confirms that the reduction of zinc starts earlier in the case of $Zn_{0.9}Fe_{0.1}O$-C, while the reoxidation of zinc begins at lower potentials than the reoxidation of iron – similar to $Zn_{0.9}Co_{0.1}O$. When fully delithiated (3.0 V), the recovered oxides exhibit a highly damped amplitude for the second coordination shell (Zn-Zn). This can be due to a (much) smaller grain size compared to the initial crystal phase and/or a significantly higher degree of disorder. The absence of an immediately apparent peak related to metallic zinc in the fully delithiated spectra further supports the high amount of reoxidized Zn (around 80%) determined *via* LCF (compare **Figure 4**).

3.5 Quantitative ex situ EXAFS Analysis

Following the qualitative discussion of the EXAFS data, we conducted also a quantitative analysis by fitting the spectra, focusing on those *ex situ* samples for which we expect the presence of metallic phases according to the findings discussed so far. The number of neighbors was fit if the improvement of the fit

was significant, and otherwise fixed to the theoretical value. Interatomic distances and the EXAFS Debye-Waller factor were fit for all paths. The amplitude reduction factors were determined to be 0.78, 0.74, 0.71, and 0.71 for Co, Fe, Zn in $Zn_{0.9}Co_{0.1}O$, and Zn in $Zn_{0.9}Fe_{0.1}O$-C, respectively, by fitting the corresponding metal references (**Table S3**) and kept constant for fitting the relevant *ex situ* spectra. The fitted EXAFS spectra are shown in **Figure S2** ($Zn_{0.9}Co_{0.1}O$) and **Figure S3** ($Zn_{0.9}Fe_{0.1}O$-C) and the fit results are tabulated in **Table S4**. **Figure 6** summarizes the results for $Zn_{0.9}Co_{0.1}O$ (**Figure 6a-f**) and $Zn_{0.9}Fe_{0.1}O$-C (**Figure 6g-i**).

Regarding the number of neighbors, the hcp crystal structure for metallic cobalt (as determined for the metal reference) corresponds to 12 nearest neighbors (purple data points in **Figure 6a** – see also **Table S3**) averaging at a distance of around 2.49 Å (see **Table S3**). The fitted coordination number for lithiated $Zn_{0.9}Co_{0.1}O$, however, is only about 6 at all given states of dis-/charge, suggesting that any Co^0 cluster formed during lithiation remains relatively small. **Figure 6b** shows that the Co-Co(Zn) interatomic distance is around 2.53 Å, and only contracts to about 2.50 Å in the fully lithiated state. The generally higher interatomic distance (with respect to the metal reference) could originate from the formation of a Co_xZn alloy. In fact, for Fe-doped and Mn-doped ZnO, the electrochemical formation of such an alloy has been reported very recently [27,36], rendering such phenomenon also likely for Co-doped ZnO – similar to the electrochemical deposition of amorphous Co_xZn alloys from molten salts electrolytes [37]. The eventual slight decrease of the interatomic distance might be the result of the incorporation of lithium into such binary alloy in the fully lithiated state and/or the very local separation into LiZn and Co^0 clusters, as observed earlier for an Sn_2Fe alloy [38]. The interatomic distance of 2.50 Å is, indeed, in good agreement with the actual averaged value for hcp-structured Co^0 (**Table S3**). The Debye-Waller factors are shown in **Figure 6c** and are around 0.01 $Å^2$ in all cases, indicating that the disorder around the cobalt atoms remains rather constant.

Metallic zinc has an hcp structure with 6 neighboring zinc atoms at a distance of around 2.66 Å and 6 additional neighboring zinc atoms at around 2.9 Å [39]. The fit of the Zn^0 reference (see **Figure S2b** and **Table S3**) is in good agreement with that, showing only a slight deviation in the second shell (2.81(4) Å vs. 2.9 Å). The EXAFS spectra at 0.55 V upon lithiation and at 1.0 V upon delithiation (**Figure 6d**) are best fit with these two Zn-Zn scattering paths and fixed coordination numbers. During the subsequent alloying reaction, the Zn coordination changes to around 7 in the fully lithiated state. Simultaneously, the fit improves by introducing a Li-Zn contribution to the theoretical model (see **Figure S5**), and the number of Zn-Li scattering contributions increases due to the formation of the Li_xZn alloy. The final Li:Zn ratio is about 4:7, corresponding to a stoichiometry of ca. $Li_{0.6}Zn$, i.e., slightly below the theoretical maximum of Li_1Zn, but well within what has been experimentally determined earlier for simple binary alloys [40]. Meanwhile, the Zn-Zn distances remain relatively constant at around 2.61 Å (**Figure 6e**), which is shorter than the Zn-Li in Li_xZn (2.7 Å, space group *Fd3m*) [41][37] and Zn-Zn in hcp Zn^0 (2.65 Å). The difference for the second Zn-Zn coordination shell of samples at 0.55 V upon lithiation and at 1.0 V upon delithiation is even greater with about 2.58(8) Å (vs. 2.81(4) Å), though with rather large error bars. Nonetheless, these findings suggest that the formed metallic zinc and its alloy crystallize in a largely distorted structure. In fact, the Debye-Waller factors are generally high, especially for the second Zn-Zn contribution. In addition to the fact that the metals are formed *via* electrochemical reduction of the oxide, the presence of ultrasmall cobalt nanograins in the direct vicinity and the partial alloying with cobalt (not considered for the discussion due to the rather high concentration of zinc and the clear appearance of metallic zinc in previous *operando* XRD experiments) may be responsible for such deviation [24,27,28].

The EXAFS fit results for the electrodes based on $Zn_{0.9}Fe_{0.1}O$-C at the Fe K-edge are presented in **Figure 6g-i**. The metallic iron reference has a bcc structure with 8 nearest neighbors at a distance of

around 2.46(2) Å and 6 additional neighbors at a distance of around 2.846(15) Å (see also the total number of neighboring Fe atoms indicated in purple in **Figure 6g**). The best fit results for the *ex situ* Fe K-edge EXAFS spectra, however, were achieved with only one Fe-Fe(Zn) scattering path for the *R* range of 1-3 Å and with a total of about 5 neighboring atoms, i.e., a much lower number compared to the theoretically expected 14 (**Figure 6g**), but similar to the findings for $Zn_{0.9}Co_{0.1}O$. Interestingly, largely decreased coordination numbers for iron have been reported very recently also for Fe-doped CeO_2, in which the iron dopant is reduced to the metallic state, while the overall crystal structure is well maintained upon lithiation [42]. The very low coordination number has accordingly been assigned to the presence of ultrasmall Fe^0 domains with only a very limited number of additional iron atoms in the direct vicinity, suggesting that the size of the metallic iron domains remains very small also for $Zn_{0.9}Fe_{0.1}O$-C. Nonetheless, the Fe-Fe(Zn) distance of around 2.51 Å initially (i.e., at 0.8 V; **Figure 6h**) is relatively close to the one of bcc-structured Fe (compare **Table S3**), indicating that at such rather high potentials very fine metallic iron clusters are formed. Upon further lithiation, the Fe-Fe(Zn) interatomic distance increases slightly to around 2.55 Å, which is in line with the formation of a Fe_xZn alloy, as found earlier by *operando* XRD and Mössbauer spectroscopy [27], before decreasing slightly to about 2.5 Å for the fully lithiated state, in agreement with the findings for the Co K-edge and potentially related to the incorporation of lithium into such binary Fe_xZn alloy and/or the local separation into LiZn and Fe^0 clusters (similar to $Zn_{0.9}Co_{0.1}O$). Moreover, the Debye-Waller factors remain constant at around 0.01 $Å^2$ (**Figure 6i**), also similar to the findings for the Co K-edge in $Zn_{0.9}Co_{0.1}O$.

Figure 6j-l display the results of the EXAFS fits at the Zn K-edge for $Zn_{0.9}Fe_{0.1}O$-C. The zinc spectrum at 0.8 V upon lithiation still exhibits the two peaks for the first (Zn-O) and second (Zn-Zn) coordination shells of ZnO (compare also **Figure 5d**), indicating that it is still predominantly oxidized. However, the coordination number of the Zn-O scattering path is reduced from 4, as theoretically expected [29], to 2

(**Figure 6j**), and the fit is substantially improved when another Zn-Zn contribution from metallic zinc at a distance of around 2.61 Å is added (see **Table S4**). This indicates that the reduction of zinc already started at such high potentials, in agreement with the XANES data. After the conversion reaction, i.e., once all zinc has been reduced to the metallic state (either in form of an alloy or as pure zinc), the results of the EXAFS fit are very comparable to $Zn_{0.9}Co_{0.1}O$ and also follow the same trend upon further lithiation (**Figure 6j-l** and **Figure S5**), indicating that the overall mechanism is essentially the same. Furthermore, in agreement with the XANES data and qualitative EXAFS analysis, metallic iron is still detectable at 1.5 V upon delithiation, while the oxidation of zinc has already started at such potential (**Figure 6g-l**).

In sum, the quantitative analysis of the *ex situ* EXAFS spectra reveals that both Co and Fe have a much smaller number of neighboring atoms compared to the thermodynamically most stable metallic phases at room temperature, which suggests a very small size of such metallic clusters. Additionally, the results confirm that iron has been completely reduced to the metallic state at 0.8 V, which triggers also the electrochemical reduction of zinc – presumably the zinc ions/atoms in the direct vicinity of such clusters. Moreover, both Co and Fe form an alloy with Zn during the electrochemical reduction, which is anticipated to further prevent any extensive Fe^0 and Co^0 cluster growth, while also confining the growth of the Zn^0 and Li_xZn domains – both exhibiting a high degree of disorder.

4. Conclusions

The comparative and complementary *ex situ* and *operando* synchrotron XAS investigation of the de-/lithiation behavior of isovalent Co-doped ZnO and aliovalent Fe-doped ZnO allowed for very detailed and valuable insights into the overall reaction mechanism, which are not accessible by conventional *operando* characterization methods: First, aliovalent Fe is reduced already at a rather early

stage of lithiation, at least partially owing to the initial Li^+ insertion, and the formation of very small Fe^0 nanograins kinetically triggers the reduction of zinc – different from isovalent Co-doped ZnO, for which the reduction of cobalt and, thus, also zinc occurs at significantly lower potentials. Second, the metallic clusters of both iron and cobalt remain very small and both form an alloy with zinc, and presumably further a ternary alloy with lithium at sufficiently low potentials. Third, the Zn^0 and Li_xZn phases formed are characterized by a high degree of disorder, which is assigned to the presence of the metallic iron and cobalt nanoclusters and their binary alloys with zinc, confining the metallic zinc and Li_xZn domains. These phenomena, finally, allow for a highly reversible formation of the corresponding metal oxides with about 80% being reoxidized under the given experimental conditions. While the reoxidation of Fe and Co, though, appear at rather high potentials, which is less suitable for practical applications as lithium-ion anodes, their presence also favors the overall de-/lithiation reaction. Accordingly, these findings may help to develop further advanced active materials based on metal oxides and alloys for lithium-ion batteries.

Supporting Information

Linear combination fitting results for XANES spectra at the Zn K-edge of $Zn_{0.9}Co_{0.1}O$ and $Zn_{0.9}Fe_{0.1}O$-C; EXAFS fitting results of the Co^0, Fe^0, and Zn^0 reference spectra; EXAFS fitting results of the metallic spectra upon de-/lithiation of $Zn_{0.9}Co_{0.1}O$ and $Zn_{0.9}Fe_{0.1}O$-C at the Co, Fe, and Zn K-edge.

Acknowledgements

The experiments were performed at the beamline BM08 “LISA” at the European Synchrotron Radiation Facility (ESRF) in Grenoble, France, and the authors are very grateful for having been granted this beam

time (08-01-962 and MA 3171). Moreover, the authors would like to deeply thank Dr. Giovanni Orazio Lepore for his dedicated and excellent support as local beamline contact. Financial support from the BMW Group, the Vector Foundation within the NEW E^2 project, as well as the Helmholtz Association is kindly acknowledged.

Conflict of Interest

The authors declare no conflict of interest.

Keywords

transition metal doping, zinc oxide, anode, lithium-ion battery, X-ray absorption spectroscopy

Data Availability Statement

The datasets generated during and/or analyzed during the current study are available from the corresponding authors on reasonable request

References

[1] B. Scrosati, J. Garche, Lithium batteries: Status, prospects and future, J. Power Sources. 195 (2010) 2419–2430. https://doi.org/10.1016/j.jpowsour.2009.11.048.

[2] M. Armand, P. Axmann, D. Bresser, M. Copley, K. Edström, C. Ekberg, D. Guyomard, B. Lestriez, P. Novák, M. Petranikova, W. Porcher, S. Trabesinger, M. Wohlfahrt-Mehrens, H. Zhang, Lithium-ion batteries – Current state of the art and anticipated developments, J. Power Sources. 479 (2020) 228708. https://doi.org/10.1016/j.jpowsour.2020.228708.

[3] D. Bresser, A. Moretti, A. Varzi, S. Passerini, The Role of Batteries for the Successful Transition to Renewable Energy Sources, Encycl. Electrochem. (2020) 1–9. https://doi.org/10.1002/9783527610426.bard110024.

[4] D. Larcher, J.M. Tarascon, Towards greener and more sustainable batteries for electrical energy storage, Nat. Chem. 7 (2015) 19–29. https://doi.org/10.1038/nchem.2085.

[5] Z. Shi, M. Liu, J.L. Gole, Electrochemical properties of Li-Zn alloy electrodes prepared by kinetically controlled vapor deposition for lithium batteries, Electrochem. Solid-State Lett. 3 (2000) 312–315. https://doi.org/10.1149/1.1391133.

[6] J. Hassoun, G. Derrien, S. Panero, B. Scrosati, A nanostructured Sn-C composite lithium battery electrode with unique stability and high electrochemical performance, Adv. Mater. 20 (2008) 3169–3175. https://doi.org/10.1002/adma.200702928.

[7] U. Kasavajjula, C. Wang, A.J. Appleby, Nano- and bulk-silicon-based insertion anodes for lithium-ion secondary cells, J. Power Sources. 163 (2007) 1003–1039. https://doi.org/10.1016/j.jpowsour.2006.09.084.

[8] W.J. Zhang, A review of the electrochemical performance of alloy anodes for lithium-ion batteries, J. Power Sources. 196 (2011) 13–24. https://doi.org/10.1016/j.jpowsour.2010.07.020.

[9] M.N. Obrovac, V.L. Chevrier, Alloy Negative Electrodes for Li-Ion Batteries, Chem. Rev. 114 (2014) 11444–11502. https://doi.org/10.1021/cr500207g.

[10] C. Liang, M. Gao, H. Pan, Y. Liu, M. Yan, Lithium alloys and metal oxides as high-capacity anode materials for lithium-ion batteries, J. Alloys Compd. 575 (2013) 246–256. https://doi.org/10.1016/j.jallcom.2013.04.001.

[11] D. Liu, Z. jiao Liu, X. Li, W. Xie, Q. Wang, Q. Liu, Y. Fu, D. He, Group IVA Element (Si, Ge, Sn)-Based Alloying/Dealloying Anodes as Negative Electrodes for Full-Cell Lithium-Ion Batteries, Small. 13 (2017) 1–27. https://doi.org/10.1002/smll.201702000.

[12] X.H. Huang, X.H. Xia, Y.F. Yuan, F. Zhou, Porous ZnO nanosheets grown on copper substrates as anodes for lithium ion batteries, Electrochim. Acta. 56 (2011) 4960–4965. https://doi.org/10.1016/j.electacta.2011.03.129.

[13] F. Belliard, J.T.S. Irvine, Electrochemical performance of ball-milled ZnO-SnO2 systems as anodes in lithium-ion battery, J. Power Sources. 97–98 (2001) 219–222. https://doi.org/10.1016/S0378-7753(01)00544-4.

[14] J. Read, D. Foster, J. Wolfenstine, W. Behl, SnO2-carbon composites for lithium-ion battery anodes, J. Power Sources. 96 (2001) 277–281. https://doi.org/10.1016/S0378-7753(00)00569-3.

[15] I.A. Courtney, J.R. Dahn, Key Factors Controlling the Reversibility of the Reaction of Lithium with SnO2 and Sn2BPO6 Glass, J. Electrochem. Soc. 144 (1997) 2943–2948. https://doi.org/10.1149/1.1837941.

[16] P. Poizot, S. Laruelle, S. Grugeon, L. Dupont, J.-M. Tarascon, Nano-sized transition-metal oxides as negative-electrode materials for lithium-ion batteries, Nature. 407 (2000) 496–499.

[17] J. Cabana, L. Monconduit, D. Larcher, M.R. Palacín, Beyond Intercalation-Based Li-Ion Batteries: The State of the Art and Challenges of Electrode Materials Reacting Through Conversion

Reactions, Adv. Mater. 22 (2010) 170–192. https://doi.org/10.1002/adma.201000717.

[18] N. Nitta, G. Yushin, High-capacity anode materials for lithium-ion batteries: Choice of elements and structures for active particles, Part. Part. Syst. Charact. 31 (2014) 317–336. https://doi.org/10.1002/ppsc.201300231.

[19] D. Bresser, S. Passerini, B. Scrosati, Leveraging valuable synergies by combining alloying and conversion for lithium-ion anodes, Energy Environ. Sci. 9 (2016) 3348–3367. https://doi.org/10.1039/C6EE02346K.

[20] C.J. Pelliccione, Y. Ding, E. V. Timofeeva, C.U. Segre, In Situ XAFS Study of the Capacity Fading Mechanisms in ZnO Anodes for Lithium-Ion Batteries, J. Electrochem. Soc. 162 (2015) A1935–A1939. https://doi.org/10.1149/2.1011509jes.

[21] Y. Yan, F. Du, X. Shen, Z. Ji, X. Sheng, H. Zhou, G. Zhu, Large-scale facile synthesis of Fe-doped SnO2 porous hierarchical nanostructures and their enhanced lithium storage properties, J. Mater. Chem. A. 2 (2014) 15875–15882. https://doi.org/10.1039/c4ta02077d.

[22] P. Nithyadharseni, K.P. Abhilash, S. Petnikota, M.R. Anilkumar, R. Jose, K.I. Ozoemena, R. Vijayaraghavan, P. Kulkarni, G. Balakrishna, B.V.R. Chowdari, S. Adams, M. V. Reddy, Synthesis and Lithium Storage Properties of Zn, Co and Mg doped SnO2 Nano Materials, Electrochim. Acta. 247 (2017) 358–370. https://doi.org/10.1016/j.electacta.2017.06.170.

[23] M. Lübke, D. Ning, C.F. Armer, D. Howard, D.J.L. Brett, Z. Liu, J.A. Darr, Evaluating the Potential Benefits of Metal Ion Doping in SnO2 Negative Electrodes for Lithium Ion Batteries, Electrochim. Acta. 242 (2017) 400–407. https://doi.org/10.1016/j.electacta.2017.05.029.

[24] D. Bresser, F. Mueller, M. Fiedler, S. Krueger, R. Kloepsch, D. Baither, M. Winter, E. Paillard, S. Passerini, Transition-Metal-Doped Zinc Oxide Nanoparticles as a new Lithium-Ion Anode Material, Chem. Mater. 25 (2013) 4977–4985. https://doi.org/10.1021/cm403443t.

[25] F. Mueller, A. Gutsche, H. Nirschl, D. Geiger, U. Kaiser, D. Bresser, S. Passerini, Iron-Doped ZnO for Lithium-Ion Anodes: Impact of the Dopant Ratio and Carbon Coating Content, J. Electrochem. Soc. 164 (2017) A6123–A6130. https://doi.org/10.1149/2.0171701jes.

[26] Y. Ma, Y. Ma, G. Giuli, T. Diemant, R.-J. Behm, D. Geiger, U. Kaiser, U. Ulissi, S. Passerini, D. Bresser, Conversion/alloying lithium-ion anodes – enhancing the energy density by transition metal doping, Sustain. Energy Fuels. 2 (2018) 2601–2608. https://doi.org/10.1039/c8se00424b.

[27] J. Asenbauer, A. Hoefling, S. Indris, J. Tübke, S. Passerini, D. Bresser, Mechanistic Insights into the Lithiation and Delithiation of Iron-Doped Zinc Oxide: The Nucleation Site Model, ACS Appl. Mater. Interfaces. 12 (2020) 8206–8218. https://doi.org/10.1021/acsami.9b19958.

[28] F. Mueller, D. Geiger, U. Kaiser, S. Passerini, D. Bresser, Elucidating the Impact of Cobalt Doping on the Lithium Storage Mechanism in Conversion/Alloying-Type Zinc Oxide Anodes, ChemElectroChem. 3 (2016) 1311–1319. https://doi.org/10.1002/celc.201600179.

[29] G. Giuli, A. Trapananti, F. Mueller, D. Bresser, F. Dácapito, S. Passerini, Insights into the Effect of Iron and Cobalt Doping on the Structure of Nanosized ZnO, Inorg. Chem. 54 (2015) 9393–9400. https://doi.org/10.1021/acs.inorgchem.5b00493.

[30] G. Giuli, T. Eisenmann, D. Bresser, A. Trapananti, J. Asenbauer, F. Mueller, S. Passerini, Structural and electrochemical characterization of Zn1-xFexO-effect of aliovalent doping on the Li+ storage mechanism, Materials. 11 (2017) 49.

[31] B. Ravel, M. Newville, ATHENA, ARTEMIS, HEPHAESTUS: data analysis for X-ray absorption spectroscopy using IFEFFIT, J. Synchrotron Radiat. 12 (2005) 537–541. https://doi.org/10.1107/S0909049505012719.

[32] S.I. Zabinsky, J.J. Rehr, A. Ankudinov, R.C. Albers, M.J. Eller, Multiple-scattering calculations of x-ray-absorption spectra, Phys. Rev. B. 52 (1995) 2995–3009.

https://doi.org/10.1103/PhysRevB.52.2995.

[33] F. Mueller, D. Bresser, V.S.K. Chakravadhanula, S. Passerini, Fe-doped SnO2 nanoparticles as new high capacity anode material for secondary lithium-ion batteries, J. Power Sources. 299 (2015) 398–402. https://doi.org/10.1016/j.jpowsour.2015.08.018.

[34] T. Eisenmann, J. Asenbauer, S.J. Rezvani, T. Diemant, R.J. Behm, D. Geiger, U. Kaiser, S. Passerini, D. Bresser, Impact of the Transition Metal Dopant in Zinc Oxide Lithium-Ion Anodes on the Solid Electrolyte Interphase Formation, Small Methods. (2021) 2001021. https://doi.org/10.1002/smtd.202001021.

[35] A.J. Bard, R. Parsons, J. Jordan, Standard Potentials in Aqueous Solution, Marcel Dekker Inc., New York and Basel, 1985. https://books.google.de/books?id=fuJV1H18KtEC.

[36] T. Eisenmann, A. Birrozzi, A. Mullaliu, G. Giuli, A. Trapananti, S. Passerini, D. Bresser, Effect of Applying a Carbon Coating on the Crystal Structure and De /Lithiation Mechanism of Mn-doped ZnO Lithium-Ion Anodes, J. Electrochem. Soc. 168 (2021) 030503.

[37] N. Koura, T. Endo, Y. Idemoto, The electrodeposition of amorphous Co-Zn alloy from ambient temperature molten salt electrolytes, J. Non. Cryst. Solids. 205–207 (1996) 650–655. https://doi.org/10.1016/S0022-3093(96)00289-X.

[38] Z. Dong, Q. Wang, R. Zhang, N.A. Chernova, F. Omenya, D. Ji, M.S. Whittingham, Reaction Mechanism of the Sn2Fe Anode in Lithium-Ion Batteries, ACS Omega. 4 (2019) 22345–22355. https://doi.org/10.1021/acsomega.9b02417.

[39] E.R. Jette, F. Foote, Precision determination of lattice constants, J. Chem. Phys. 3 (1935) 605–616. https://doi.org/10.1063/1.1749562.

[40] J. Wang, P. King, R.A. Huggins, Investigations of binary lithium-zinc, lithium-cadmium and lithium-lead alloys as negative electrodes in organic solvent-based electrolyte, Solid State Ionics.

20 (1986) 185–189. https://doi.org/10.1016/0167-2738(86)90212-2.

[41] K. Kuriyama, S. Saito, K. Iwamura, Ultrasonic study on the elastic moduli of the NaTl (B32) structure, J. Phys. Chem. Solids. 40 (1979) 457–461. https://doi.org/10.1016/0022-3697(79)90062-3.

[42] Y. Ma, Y. Ma, G. Giuli, H. Euchner, A. Groß, G.O. Lepore, F. D'Acapito, D. Geiger, J. Biskupek, U. Kaiser, H.M. Schütz, A. Carlsson, T. Diemant, R.J. Behm, M. Kuenzel, S. Passerini, D. Bresser, Introducing Highly Redox-Active Atomic Centers into Insertion-Type Electrodes for Lithium-Ion Batteries, Adv. Energy Mater. 10 (2020) 2000783. https://doi.org/10.1002/aenm.202000783.

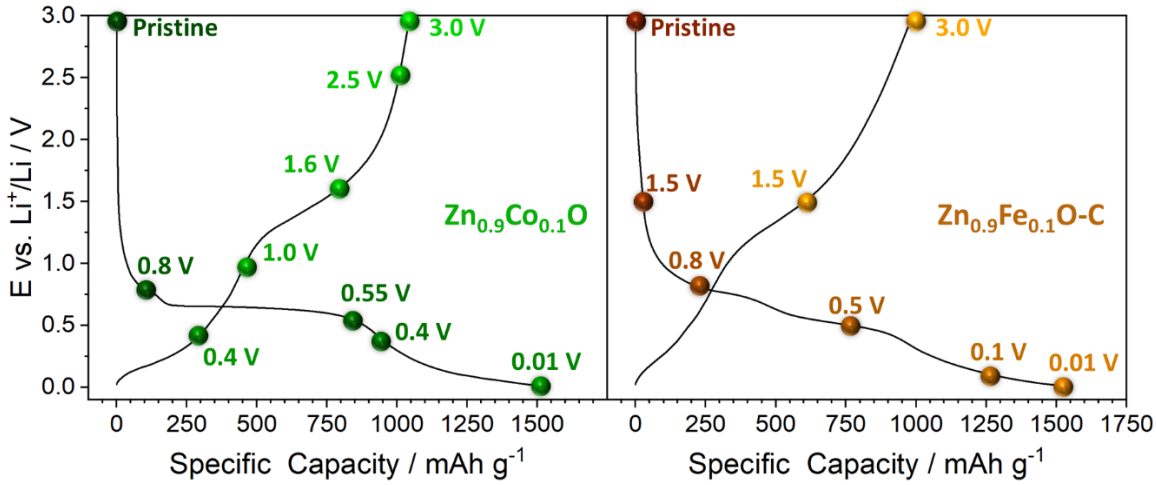

Figure 1. *First cycle dis/charge profiles of electrodes based on $Zn_{0.9}Co_{0.1}O$ (left panel) and $Zn_{0.9}Fe_{0.1}O$-C (right panel) cycled in half-cell configuration (specific current: 50 mA g^{-1}). The given potential values indicate the cut-offs at which the cells were stopped for the ex situ XAS measurements. The capacity values provided for $Zn_{0.9}Fe_{0.1}O$-C are based on the mass of the Fe-doped ZnO only, i.e., excluding the mass of the carbon coating.*

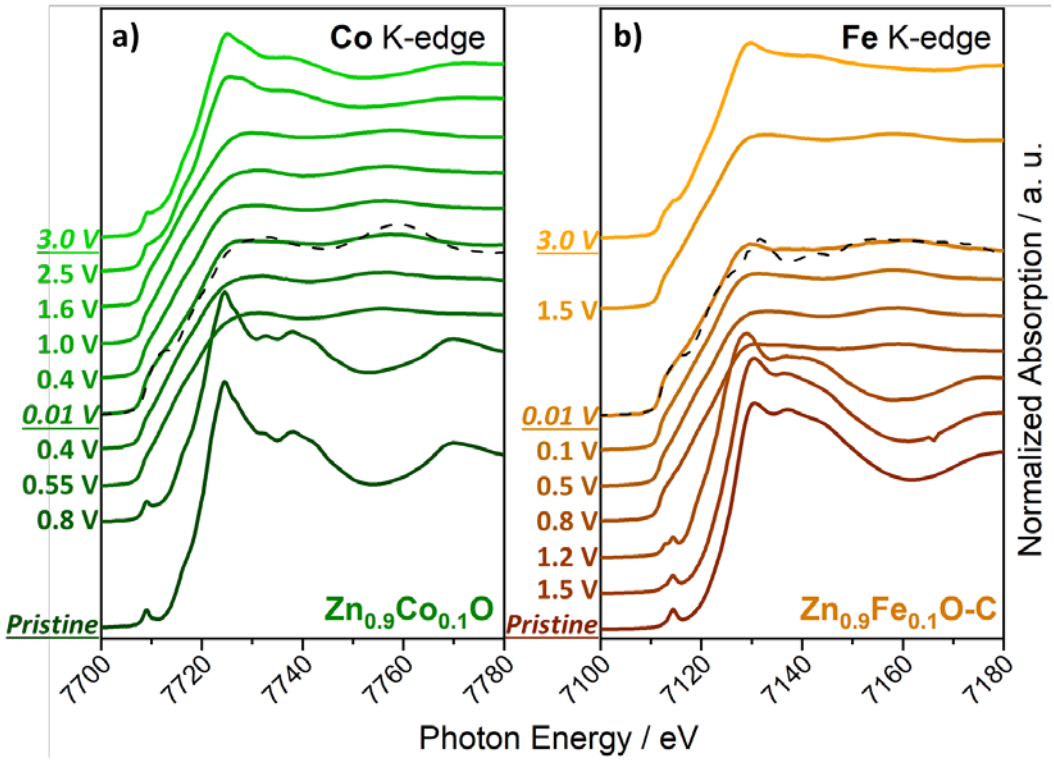

Figure 2. *Ex situ XANES spectra at (a) the Co K-edge and (b) the Fe K-edge for electrodes based on* $Zn_{0.9}Co_{0.1}O$ *and* $Zn_{0.9}Fe_{0.1}O$*-C, respectively, recorded at the indicated potential values (see also* ***Figure 1****); also shown are the reference spectra obtained for metallic* Co^0 *and* Fe^0 *(black dashed lines) along with the spectra at 0.01 V. The spectra were shifted vertically for the sake of clarity.*

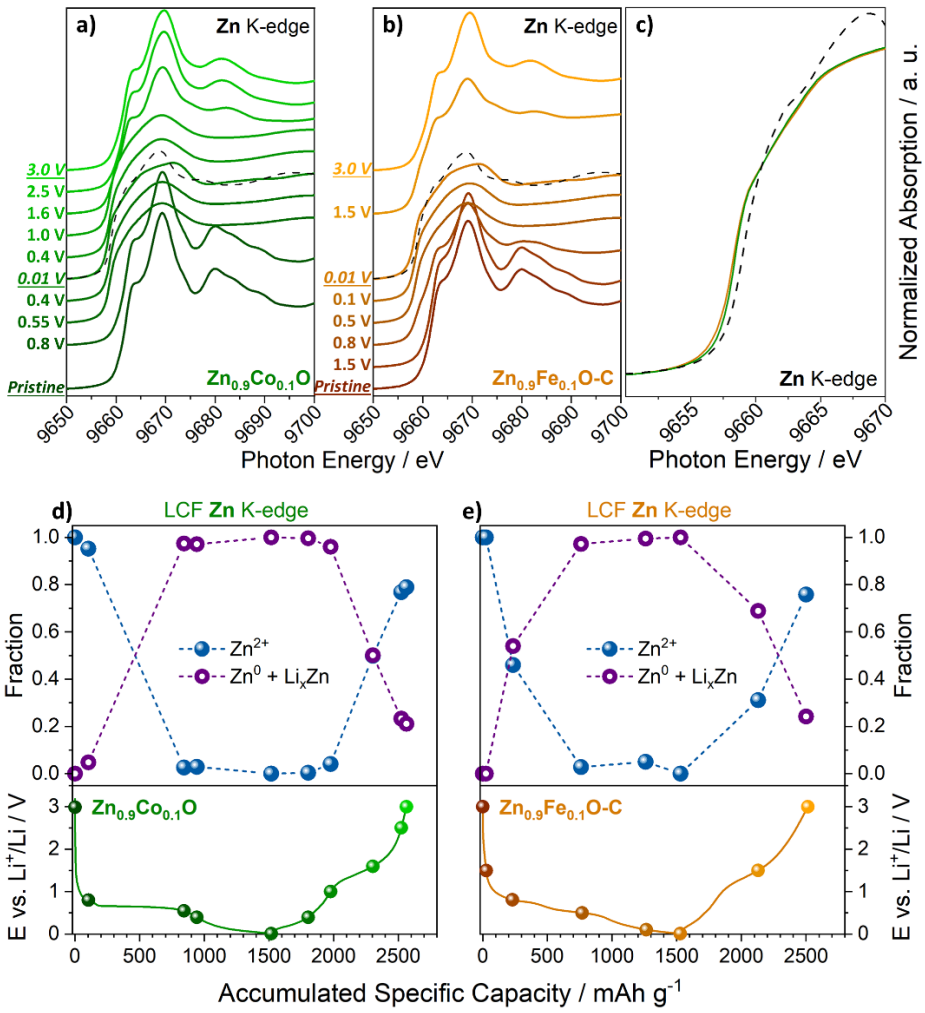

Figure 3. *(a,b) Ex situ XANES spectra at the Zn K-edge for electrodes based on (a) $Zn_{0.9}Co_{0.1}O$ (in green) and (b) $Zn_{0.9}Fe_{0.1}O$-C (in orange), recorded at the indicated potential values (see also* ***Figure 1****); also shown are the reference spectra obtained for metallic Zn^0 (black dashed lines) along with the spectra at 0.01 V. The spectra were shifted vertically for the sake of clarity. (c) Magnified comparison of the Zn K-edge spectra of fully lithiated electrodes based on $Zn_{0.9}Co_{0.1}O$ and $Zn_{0.9}Fe_{0.1}O$-C as well as the metallic Zn^0 reference (dashed black line). (d,e) Results of the LCF of the ex situ XANES data obtained for (d) $Zn_{0.9}Co_{0.1}O$ and (e) $Zn_{0.9}Fe_{0.1}O$-C, indicating the fraction of oxidized Zn^{2+} (in blue) and metallic zinc, i.e., Zn^0 + Li_xZn (in purple); in the bottom the corresponding data points along the de-/lithiation profile are shown for the reader's convenience.*

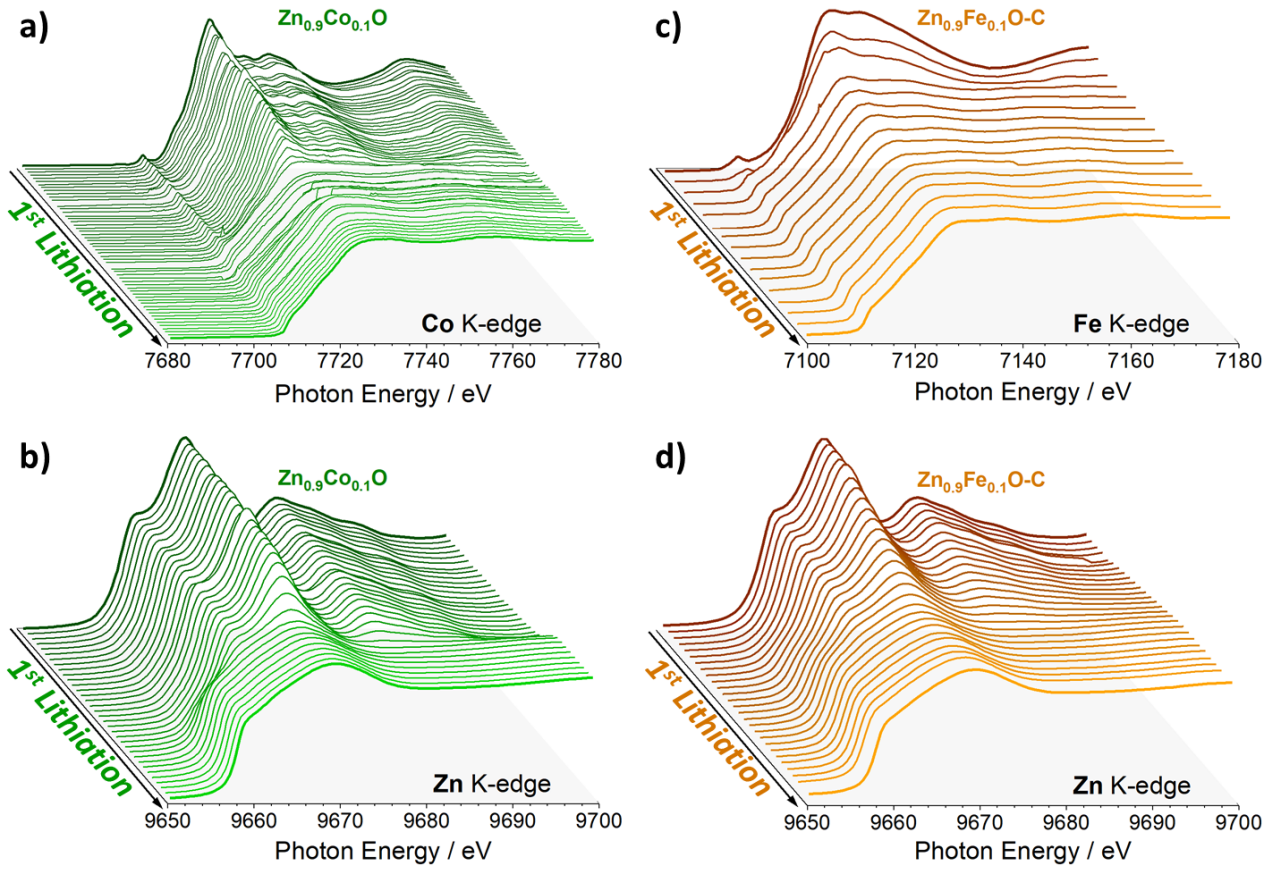

Figure 4. *Operando XANES measurements for the first lithiation of electrodes based on (a,b) $Zn_{0.9}Co_{0.1}O$ (in green) and (c,d) $Zn_{0.9}Fe_{0.1}O$-C (in orange): (a) Co K-edge, (b) Zn K-edge of $Zn_{0.9}Co_{0.1}O$, (c) Fe K-edge, and (d) Zn K-edge of $Zn_{0.9}Fe_{0.1}O$-C.*

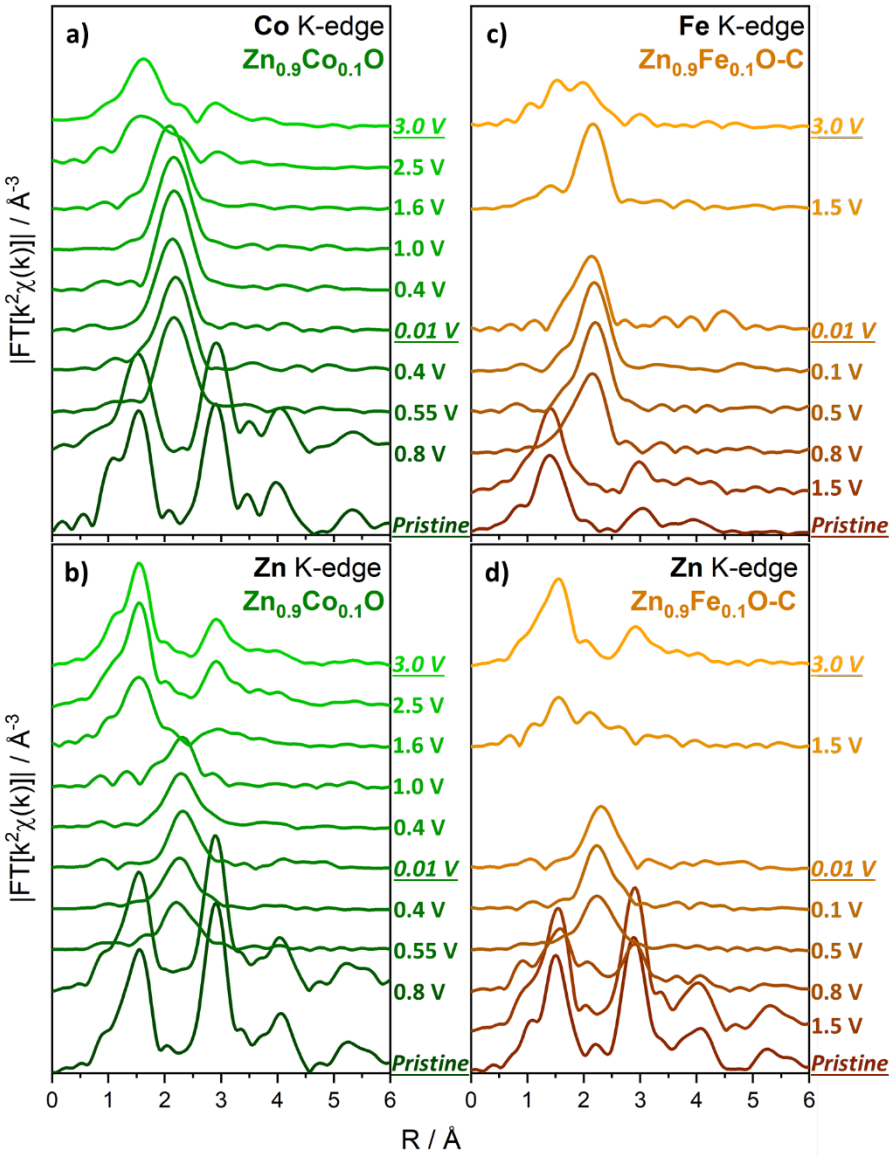

Figure 5. *Fourier transform of the $k^2\chi(k)$ ex situ EXAFS spectra collected at (a) the Co K-edge and (b) the Zn K-edge of $Zn_{0.9}Co_{0.1}O$ and at (c) the Fe K-edge and (d) the Zn K-edge of $Zn_{0.9}Fe_{0.1}O$-C. The spectra are shifted vertically for the sake of clarity.*

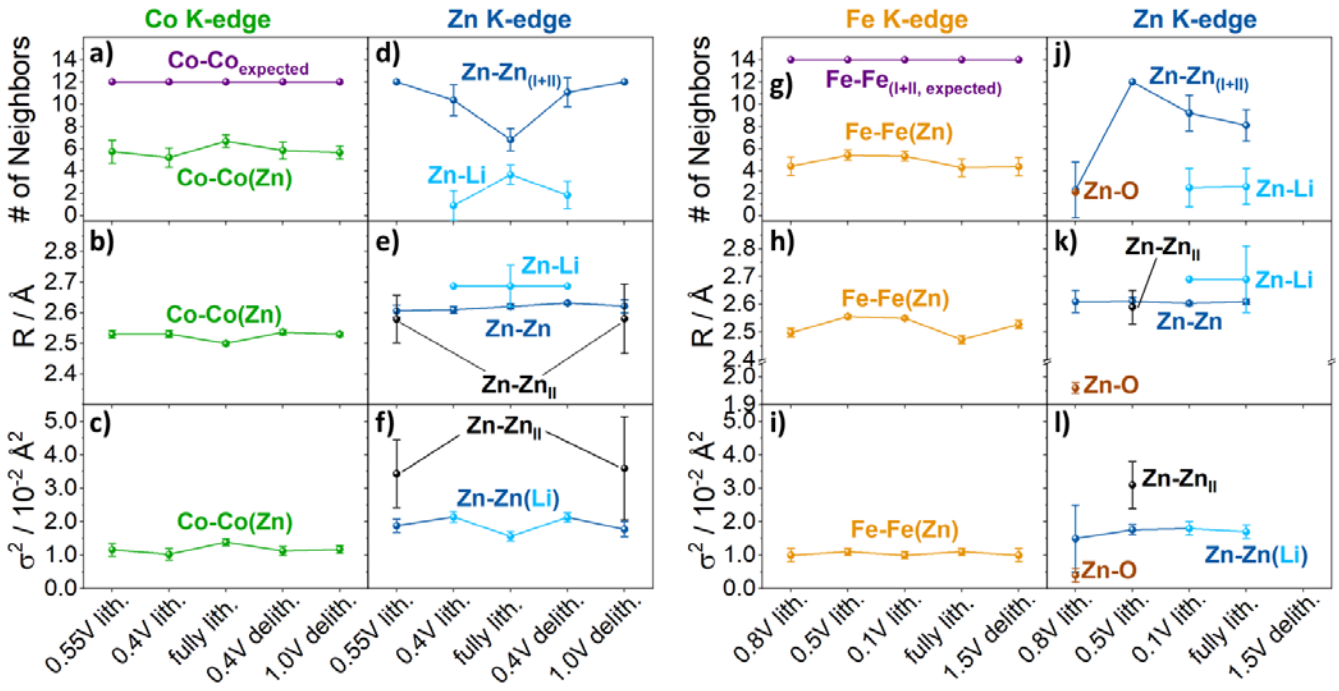

Figure 6. *Summary of the results of the ex situ EXAFS fits for electrodes based on (a-f) $Zn_{0.9}Co_{0.1}O$ and (g-l) $Zn_{0.9}Fe_{0.1}O$-C: The number of neighboring atoms are shown in the top row for each metal and compound, the interatomic distances are presented the middle row, and the Debye-Waller factors are depicted in the bottom row. The fit results for Co K-edge spectra are kept in green, the results for the Fe K-edge spectra are provided in orange, and the results for the Zn K-edge spectra are presented in blue (darker for Zn-Zn and lighter for Zn-Li) and black. The theoretically expected total of neighboring atoms for metallic (a) Co (fcc) and (g) Fe (bcc) for the coordination shells in an R-range of 1-3 Å are shown in purple for comparison.*